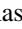



Mean-field study of the Bose-Hubbard model in the Penrose lattice

Rasoul Ghadimi ¹, Takanori Sugimoto,^{1,2} and Takami Tohyama ¹

¹*Department of Applied Physics, Tokyo University of Science, Tokyo 125-8585, Japan*

²*Advanced Science Research Center, Japan Atomic Energy Agency, Tokai, Ibaraki 319-1195, Japan*



(Received 14 May 2020; revised 8 November 2020; accepted 19 November 2020; published 7 December 2020)

We examine the Bose-Hubbard model in the Penrose lattice based on inhomogeneous mean-field theory. Since the averaged coordination number in the Penrose lattice is four, the mean-field phase diagram consisting of the Mott insulator (MI) and superfluid (SF) phase is similar to that of the square lattice. However, the spatial distribution of the Bose condensate in the SF phase is significantly different from uniform distribution in the square lattice. We find a fractal structure in its distribution near the MI-SF phase boundary. The emergence of the fractal structure is a consequence of the cooperative effect between quasiperiodicity in the Penrose lattice and criticality at the phase transition.

DOI: [10.1103/PhysRevB.102.224201](https://doi.org/10.1103/PhysRevB.102.224201)

I. INTRODUCTION

Quasicrystals have aperiodic structure different from fully disordered ones. Although translational symmetry is absent, the presence of sharp spots in Bragg reflection indicates long-range order [1,2]. Quasicrystals can be realized even in bilayer graphene [3] and photonic lattices [4]. In addition to various characteristics due to aperiodicity [5,6], recent findings expand the field of quasicrystal to include superconductivity [7–10], quantum criticality [11,12], and topology [13–17]. In general, self-similarity in quasicrystals dictates fractal structure in wave functions and phase diagrams [18,19]. This characteristic is justified by the presence of the inflation and deflation rules to construct quasicrystals [20].

One of the well-known two-dimensional quasicrystals is the so-called Penrose lattice [21,22]. One can construct the lattice using inflation, projection, or multigrade rules. The Penrose lattice has been studied intensively [23–32] and its structure dictates thermodynamically degenerate states in the energy spectrum [33,34].

Ultracold gases in optical lattices provide us an ideal playground of strong correlation [35] and also quasicrystals [36–41], which allows us to investigate the interplay of strong correlation and aperiodicity. A typical strongly correlated system in an optical lattice is the Bose-Hubbard model, where a phase transition between the Mott insulator (MI) to superfluid (SF) phase appears [42,43] as experimentally observed [44,45]. The Bose-Hubbard model is also used to describe the effective low-energy theory of superconducting films and arrays of Josephson junctions [46–48]. Recent achievements in establishing an eightfold rotationally symmetric optical lattice attract attention [49] in connection with theoretical investigation of an extended Bose-Hubbard with quasicrystalline confined potential [50], where spontaneous breaking of underlying eightfold symmetry is observed. However, the effect of aperiodicity in the Bose-Hubbard model is not yet fully understood both theoretically and experimentally.

In this paper, we investigate the phase diagram of the Bose-Hubbard model in the Penrose lattice. We use a self-consistent mean-field theory and find that the distribution of Bose condensate in the Penrose lattice exhibits a fractal structure near the MI-SF boundary. We attribute the appearance of the fractal structure to a consequence of the divergence of correlation length seen in any phase transition. Therefore, the fractal structure is a common signature of continuous phase transition in quasiperiodic systems.

The arrangement of this paper is as follows. In Sec. II, we describe our Bose-Hubbard model on the Penrose lattice and mean-field treatment. The classification of lattice sites (vertices) is also introduced. In Sec. III, we discuss the result of phase diagram, local SF amplitude, and a critical behavior of several quantities. A fractal structure near the phase transition in the perpendicular space in the Penrose lattice is also discussed. Finally, a summary is given in Sec. IV.

II. MODEL AND METHOD

The Hamiltonian of the single-band Bose-Hubbard model is defined by

$$H_{\text{BH}} = -J \sum_{(i,j)} (\hat{b}_i^\dagger \hat{b}_j + \hat{b}_j^\dagger \hat{b}_i) - \mu \sum_i \hat{n}_i + \frac{U}{2} \sum_i \hat{n}_i (\hat{n}_i - 1), \quad (1)$$

where \hat{b}_i and \hat{b}_i^\dagger are annihilation and creation operators of bosons at site i and the number operator $\hat{n}_i = \hat{b}_i^\dagger \hat{b}_i$. We refer the site to vertex, which is denoted by circles in Fig. 1(a). The summation (i, j) represents all pairs of vertices that form a link in the Penrose lattice shown as short bar connecting two vertices in Fig. 1(a). J , μ , and U in Eq. (1) are the hopping energy of boson, the chemical potential, and on-site Coulomb interaction, respectively. We note that hopping processes with the shortest intervortex distance, for example, hopping between numbers 8 and 9 in Fig. 1(a), are not included in

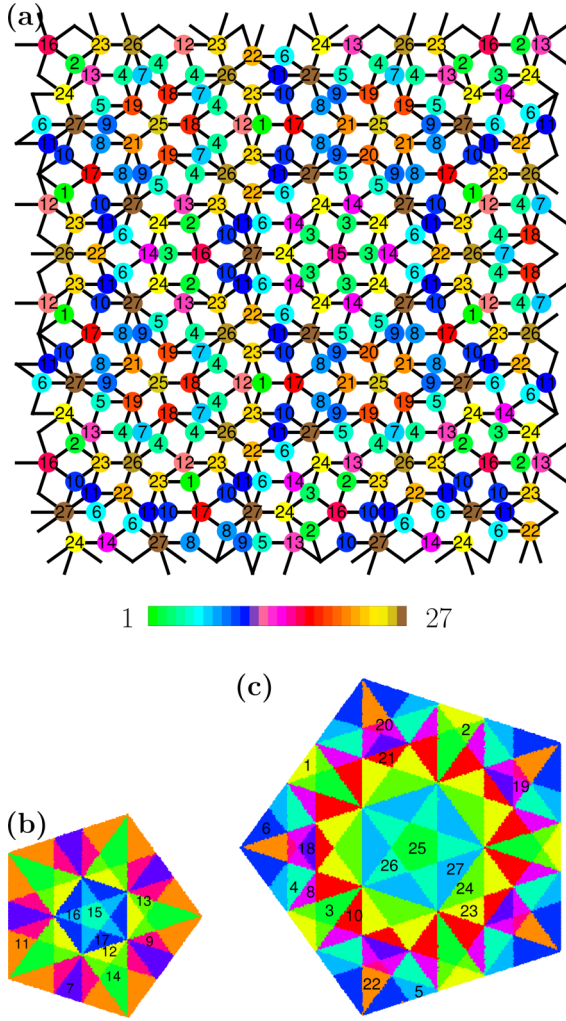


FIG. 1. (a) Part of Penrose lattice. The number and color in each vertex indicate the index α of vertices among 27 different kinds of vertices. (b) Perpendicular space of Penrose lattice for $\mathcal{Z} = 1$ and (c) that for $\mathcal{Z} = 2$. The number is the same as (a). Different colors in (b) and (c) distinguish different sections in perpendicular space.

Eq.(1). This exclusion guarantees bipartite properties of this Penrose lattice.

Because of the presence of the hopping term in Eq. (1), the exact solution is inaccessible. Therefore, we use a mean-field technique and decouple the hopping term using local SF amplitude $\langle \hat{b}_i \rangle$. The resulting mean-field Hamiltonian is given by $H_{\text{MF}} = \sum_i H_i + E_0$ with

$$H_i = -J(\psi_i^* \hat{b}_i + \text{H.c.}) - \mu \hat{n}_i + \frac{U}{2} \hat{n}_i (\hat{n}_i - 1), \quad (2)$$

where $\psi_i = \sum_j \langle \hat{b}_j \rangle$ with summation over vertices connected to the vertex i by a link and $E_0 = J \sum \psi_i^* \langle \hat{b}_i \rangle$.

To obtain a self-consistent solution of Eq. (2) in the local Hilbert space containing maximally n_b bosons, we start with an initial ψ_i and then calculate $\langle \hat{n}_i \rangle$ and $\langle \hat{b}_i \rangle$ using the ground-state wave function for each vertex. We continue updating ψ_i until the convergence of $\langle \hat{n}_i \rangle$ and $\langle \hat{b}_i \rangle$ is obtained within a certain tolerance (10^{-9} in our case). This self-consistent procedure gives rise to site-dependent distribution of $\langle \hat{n}_i \rangle$ and

$\langle \hat{b}_i \rangle$ on the Penrose lattice. This technique is sometimes called inhomogeneous mean-field theory [51,52], which gives equivalent results with variational Gutzwiller method [53–60]. We note that this self-consistent procedure gives moderately consistent results compared by quantum Monte Carlo simulations in determining the phase diagram of the Bose-Hubbard model with nearest neighbor repulsion interaction [61].

We take $n_b = 7$. Within our mean-field theory, we generally find the MI and SF phases in the Bose-Hubbard model. In the MI phase, all sites have equal integer number of bosons and thus $\langle \hat{b}_i \rangle = 0$. On the other hand, $\langle \hat{b}_i \rangle$ is nonzero for the SF phase. In our method, we find order parameters on all vertices. Therefore, we can check the existence of exotic states like Bose-glass, supersolid, and density-wave phases. We did not see these phases in our model. This is reasonable because the Bose glass usually needs any disorders and a lack of intervertex interactions in our model should make the supersolid and density wave unstable [52,57,62]. To minimize the boundary effects, we apply periodic boundary conditions (PBC) in an approximant of Penrose lattice containing $N = 167761$ vertices (for details, see the Appendix) [63–65].

In the Penrose lattice, a classification of vertices based on local environment is useful. For this classification, we first label vertices with their coordination number M , i.e., the number of different paths using one link from a given vertex. This is shown in Figs. 2(a) and 2(b) by numbers on vertices of Penrose lattice. We can find that $M \in \{3, 4, 5, 6, 7\}$. Therefore, all vertices can be classified into five different classes using their coordination number. Next, we define $m_{k=1}^{(l)}$ as the number of one-linked path ($k = 1$) connecting from a given vertex to vertices labeled with $l \in \{3, 4, 5, 6, 7\}$. For instance, consider central vertex highlighted by a blue disk in Fig. 2(a). It is easy to check that there are (is) six vertices (one vertex) labeled with 3 (5) connected by one link from the central vertex, which are highlighted by blue color for both links and vertices in Fig. 2(b). Using a set of $m_1^{(l)}$, we can subdivide vertices of the same coordination number M . For this propose, we relabel all vertices with

$$(m_1^{(3)}, m_1^{(4)}, m_1^{(5)}, m_1^{(6)}, m_1^{(7)}),$$

leading to 14 kinds of vertices with different sets of $m_1^{(l)}$:

$$\begin{aligned} & (0, 0, 3, 0, 0), \quad (0, 1, 1, 1, 0), \quad (0, 1, 1, 0, 1), \quad (0, 0, 2, 1, 0), \\ & (0, 0, 2, 0, 1), \quad (2, 0, 2, 0, 0), \quad (5, 0, 0, 0, 0), \quad (4, 0, 1, 0, 0), \\ & (4, 0, 0, 1, 0), \quad (3, 1, 0, 1, 0), \quad (2, 2, 0, 0, 1), \quad (0, 0, 5, 0, 0), \\ & (3, 0, 3, 0, 0), \quad (6, 0, 1, 0, 0). \end{aligned} \quad (3)$$

For instance, the central vertex labeled with 7 ($M = 7$) in Fig. 2(b) is relabeled with $(6, 0, 1, 0, 0)$, and the $M = 5$ vertex located the left hand side of the $M = 7$ vertex is relabeled with $(2, 2, 0, 0, 1)$. Other sets of $m_1^{(l)}$ not listed in Eq. (3) are absent in the Penrose lattice. Note that different sets of $m_1^{(l)}$ mean different local environments obtained by only one link.

We can further subdivide vertices by using longer paths. For this, let us consider paths from a given vertex using two links. We define $m_{k=2}^{(l)}$ as the number of the two-link paths that connect the given vertex to vertices with coordination number $M = l$. As an example, we show in Fig. 2(c) all 23 paths obtained by using two links from the central vertex with

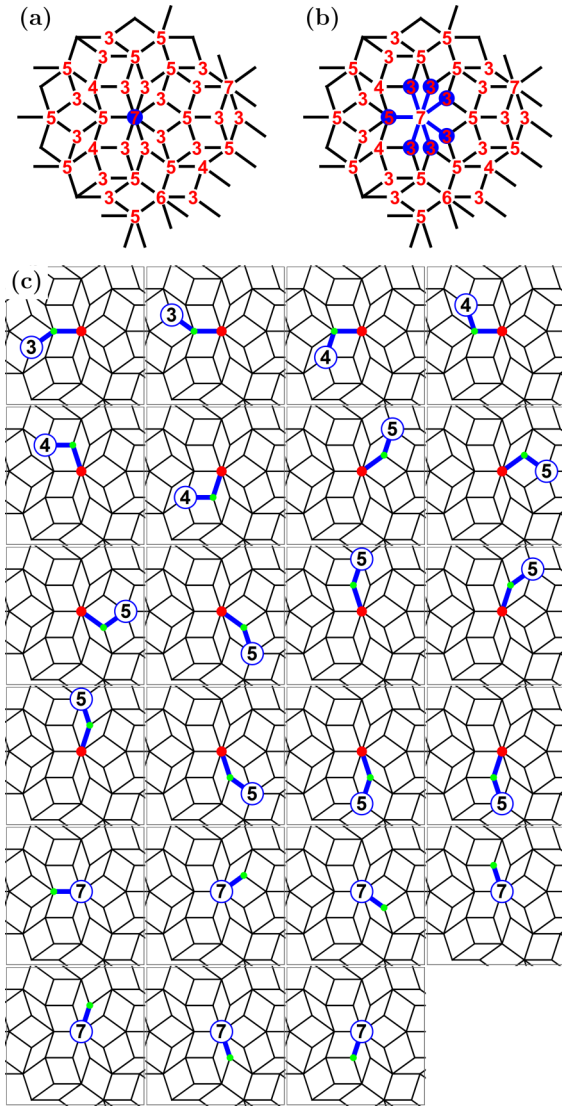


FIG. 2. (a) Part of Penrose lattice. Vertices are labeled with coordination number M . The central site with $M = 7$ is shown by a blue disk. (b) The same as (a) but all one-link paths and their end vertices from the central $M = 7$ vertex are highlighted with blue bars and disks. (c) All possible two-link paths from the central $M = 7$ vertex. There are 23 panels. The two links are denoted by blue bars. The red and green dots indicate the central vertex and vertex accessed by the one link, respectively. The number on vertices accessed by the two links indicates the coordination number on the vertices. Panels in two rows from the bottom represent the cases where the two links are the same, i.e., the starting vertex and the end vertex are the same.

$M = 7$ in Fig. 2(a). Then we can introduce labeling using both $m_{k=1}^{(l)}$ and $m_{k=2}^{(l)}$,

$$(m_1^{(3)}, m_1^{(4)}, m_1^{(5)}, m_1^{(6)}, m_1^{(7)}, m_2^{(3)}, m_2^{(4)}, m_2^{(5)}, m_2^{(6)}, m_2^{(7)}).$$

For instance, using Fig. 2(b) for $m_{k=1}^{(l)}$ and Fig. 2(c) for $m_{k=2}^{(l)}$, we can label the central vertex with $M = 7$ in Fig. 2(a) with $(6,0,1,0,0,2,4,10,0,7)$. Performing this procedure for all vertices in the supercell of Penrose approximant with PBC, we find that there are 27 kinds of vertices with different sets of $m_{k=1}^{(l)}$ and $m_{k=2}^{(l)}$, by which almost the whole system is covered.

This means that there are 27 types of vertices when we focus on two-link paths. These 27 sets of $m_{k \leq 2}^{(l)}$ are listed in Table I, where we define $\alpha (= 1, 2, \dots, 27)$ to label different sets. The coordination number of each set, M , is presented in the second row of Table I, while $m_1^{(k)}$ are shown in the third to seventh rows. It is easy to check that there is only 14 different sets for $m_{k=1}^{(l)}$ in Table I as in Eq. (3). Vertex configuration using two-link paths, $m_{k=2}^{(l)}$ is given in the eighth–12th rows of Table I. We note that, in our approximant periodic lattice with $N = 167761$ vertices, there are vertices that do not belong to the 27 types around defects, but we can ignore them since the total number of the defects is just 2.

Even for longer paths using more than two links, we can also define $m_k^{(l)}$ for $k > 2$. Using these $m_k^{(l)}$, we further classify vertices with different types. We call the number of distinct vertices for a given k the number of classes (NoC). For example, NoC is equal to 5, 14, and 27 for $k = 0, 1$, and 2, respectively. Note that NoC = 5 for $k = 0$ corresponds to the five sets of the coordination number M . We draw a small portion of Penrose lattice in Fig. 1(a), where each vertex has an index $\alpha (= 1, 2, \dots, 27)$ and color indicating its class obtained for $k = 2$. We can increase k as many as possible. We find $\text{NoC} \propto k^{1.84}$ in the large k region (discussed below). We will come back to this point later.

Vertex coordinates in the Penrose lattice can be found by using the cut and projection method from five-dimensional hypercubic lattice [28] (see the Appendix for more details). In this method, we first distinguish two-dimensional real space accommodating the Penrose lattice and three-dimensional complementary space perpendicular to the real space. The orthonormal unit vectors of these spaces are on the skew with respect to the primitive vectors of five-dimensional hypercubic lattice. With an appropriate skew, we can find every vertex of the Penrose lattice in projected vertices of the hypercubic lattice into the real space, while improper vertices are also included. To eliminate these improper vertices, we use the perpendicular space as follows. Before projecting a vertex into the real space, we consider projection of the vertex into the perpendicular space. If the projected vertex is not located inside a specific rhombic icosahedron defined in the perpendicular space (see the Appendix for the exact definition), we exclude the vertex from the five-dimensional hypercubic lattice. In this manner, we can eliminate the improper vertices in advance. Therefore, every proper vertex corresponding to the Penrose lattice is located inside the rhombic icosahedron when we project it into the perpendicular space.

Interestingly, the projected vertices into the perpendicular space are located on only four pentagonal planes in the rhombic icosahedron, which we label with $\mathcal{Z} = 1, 2, 3, 4$ along the axis perpendicular to the planes [see Figs. 1(b) and 1(c) for $\mathcal{Z} = 1$ and 2, respectively]. Furthermore, the perpendicular space, namely the four pentagons, can help us to classify the vertices in the same manner explained above, i.e., the set of $m_k^{(l)}$ as local environments of the vertices. We can divide perpendicular space into symmetric sections, where each section represents vertices with a similar local environment or equivalently $m_k^{(l)}$. Therefore, one notices the index α in Fig. 1(a) mapped to different sections in the perpendicular space [see Figs. 1(b) and 1(c)]. We note that Penrose lattice's bipartite

TABLE I. Link configuration of distinct vertices in Penrose lattice. Listed are index α determined in the present work, coordination number, M , the number of vertices having l links, to which one can access using k links, $m_k^{(l)}$ ($l = 3, 4, 5, 6, 7$).

α	1	2	3	4	5	6	7	8	9	10	11	12	13	14	15	16	17	18	19	20	21	22	23	24	25	26	27
M	3	3	3	3	3	3	3	3	3	3	3	4	4	4	5	5	5	5	5	5	5	5	5	5	5	6	7
$m_1^{(3)}$	0	0	0	0	0	0	0	0	0	0	0	2	2	2	5	5	5	4	4	4	4	4	3	2	0	3	6
$m_1^{(4)}$	0	0	0	1	1	1	0	0	0	0	0	0	0	0	0	0	0	0	0	0	0	0	1	2	0	0	0
$m_1^{(5)}$	3	3	3	1	1	1	2	2	2	2	2	2	2	2	0	0	0	1	1	1	1	0	0	0	5	3	1
$m_1^{(6)}$	0	0	0	1	0	0	1	0	0	0	0	0	0	0	0	0	0	0	0	0	0	1	1	0	0	0	0
$m_1^{(7)}$	0	0	0	0	1	1	0	1	1	1	1	0	0	0	0	0	0	0	0	0	0	0	0	1	0	0	0
$m_2^{(3)}$	11	10	9	9	12	12	11	15	14	14	13	6	5	4	0	0	0	0	0	0	0	3	5	10	20	10	2
$m_2^{(4)}$	2	3	4	0	0	0	0	0	0	1	1	4	5	6	0	0	0	2	2	2	0	2	0	0	0	4	4
$m_2^{(5)}$	0	0	0	6	4	3	5	2	3	1	1	2	2	2	15	13	11	11	11	11	13	9	12	11	5	4	10
$m_2^{(6)}$	2	1	0	0	0	1	0	0	0	1	2	4	2	0	0	0	0	4	2	0	0	0	0	0	0	6	0
$m_2^{(7)}$	0	1	2	0	0	0	0	0	0	0	0	0	2	4	0	2	4	0	2	4	4	4	2	0	0	0	7

property leads to $\mathcal{Z} = 1, 3$, and $\mathcal{Z} = 2, 4$ belong to different subsystems, though the same α is shared among them.

III. RESULTS

We first examine the phase diagram of the Bose-Hubbard model on the Penrose lattice. From the calculation of two order parameters per vertex, $\langle \hat{n}_i \rangle$ and $\langle \hat{b}_i \rangle$, for the Bose-Hubbard model without disorder and/or inter-site interaction, we expect two phases: one is MI with $\langle \hat{b}_i \rangle = 0$ and $\langle \hat{n}_i \rangle = n_0$ ($n_0 = 1, 2, \dots$, corresponding to bosonic occupation number at each vertex), and the other is SF with $\langle \hat{b}_i \rangle \neq 0$. In fact, we find none of Bose-glass, density wave, and supersolid phases in the phase diagram. Figure 3 shows the phase diagram, where we find MI phases denoted by MI_{n_0} and SF. Since averaged coordination number in the Penrose lattice is $\bar{z} = 4$, which is the same as the coordination number $z = 4$ in the square lattice, the phase boundary between MI and SF is expected to be similar to that of the square lattice. This is the case as shown by the dashed orange curve along MI lobes in Fig. 3, which is the mean-field phase boundary for the square lattice given analytically [66,67] by

$$zJ_c/U = \frac{-\frac{\mu}{U} - \left(\frac{\mu}{U}\right)^2 + s + 2\frac{\mu}{U}s - s^2}{1 + \frac{\mu}{U}}, \quad (4)$$

where $s = \text{round}(\mu/U + 1/2)$. The similarity indicates small effect of aperiodicity on the phase boundary.

In the SF phase of square lattice, the local SF amplitude $\langle \hat{b}_i \rangle$ is uniform, i.e., independent of i , for any region in the phase diagram. On the other hand, nonuniform distribution of $\langle \hat{b}_i \rangle$ in the Penrose lattice is easily expected from the presence of different types of vertices as shown in Fig. 1(a). Then, an arising question is how its nonuniform distribution changes in the phase diagram. To see this, we define an α -dependent average of $\langle \hat{b}_i \rangle$ as $\bar{b}_\alpha = N_\alpha^{-1} \sum_{i \in \alpha} \langle \hat{b}_i \rangle$, where N_α is the number of α -type vertex in the whole lattice. This quantity can distinguish the 27 classes of vertices. However, each class should have further internal structure coming from possible extension of NoC for $k \geq 3$. To recognize this structure, we

also define a mean deviation of local SF amplitude distribution as $\delta b_\alpha = \sqrt{N_\alpha^{-1} \sum_{i \in \alpha} (\langle \hat{b}_i \rangle - \bar{b}_\alpha)^2}$.

With approaching phase transition from the SF side, the average value of local SF amplitude, $\bar{b} = \sum_i \langle \hat{b}_i \rangle / N$ with $N = \sum_\alpha N_\alpha$, reduces its value toward zero as shown in the inset of Fig. 4(a). At the same time, both \bar{b}_α and $\delta \bar{b}_\alpha$ become smaller. Therefore, we use $\delta \bar{b}_\alpha / \bar{b}$ to evaluate the magnitude

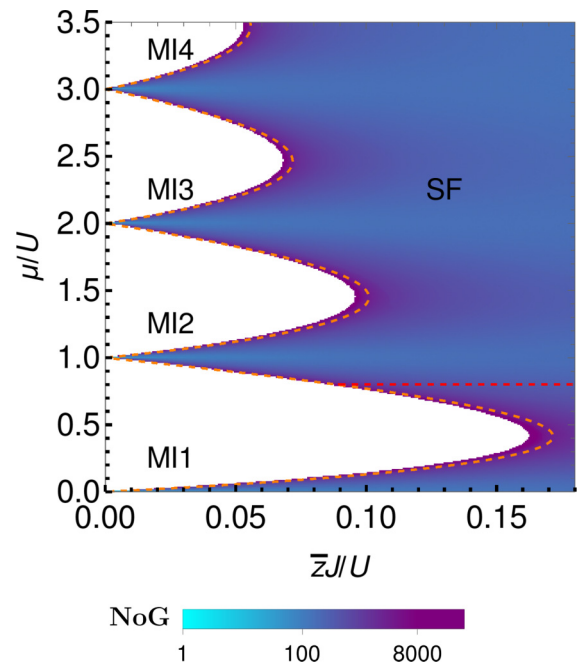


FIG. 3. Phase diagram of the Bose-Hubbard model on the Penrose lattice. The white area with the shape of lobes corresponds to the MI phase with n_0 bosons in all vertices, denoted by MI_{n_0} ($n_0 = 1, 2, \dots$). In the SF phase, the number of gap (NoG) for a threshold value of 10^{-7} defined in the text is plotted with color scale. The analytical MI-SF mean-field phase boundary for the square lattice in Eq. (4) is plotted by the orange dashed curve.

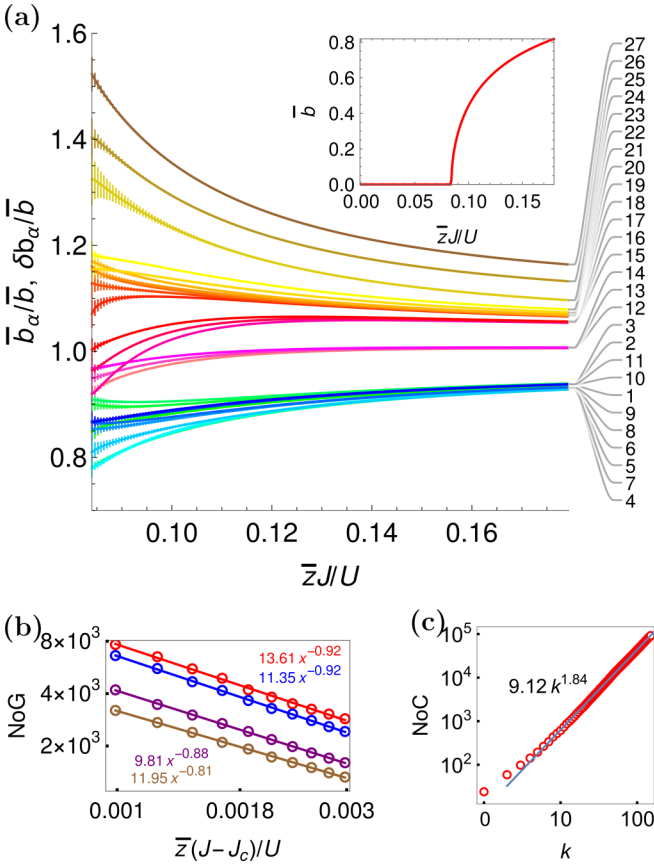


FIG. 4. (a) Averaged order parameters \bar{b}_α/\bar{b} and mean deviation $\delta b_\alpha/\bar{b}$ as a function of $\bar{z}J/U$ along the horizontal dotted line ($\mu/U = 0.8$) in Fig. 3. The colored curves represent \bar{b}_α/\bar{b} . The bars centered at each curve represent $\delta b_\alpha/\bar{b}$. The color scheme is the same as Fig. 1(a) and the number denoted at the right-hand side indicates each class α as shown in Fig. 1(a). Inset shows averaged order parameter \bar{b} . (b) Log-log plot of the number of gaps (NoG) defined in the text as a function of $\bar{z}(J - J_c)/U$ along the horizontal dotted line in Fig. 3. The brown, purple, blue, and red circles represent NoG for threshold values of 10^{-5} , 5×10^{-6} , 10^{-6} , 5×10^{-7} , respectively. The lines represent fitting function denoted by the corresponding color, where $x = \bar{z}(J - J_c)/U$. (c) Log-log plot of the number of classes (NoC) as a function of the number of links k . The blue line represents a fitting function shown in the figure.

of the mean deviation of $\delta\bar{b}_\alpha$. Note that the larger $\delta b_\alpha/\bar{b}$ is, the deeper the internal structure is.

In Fig. 4(a), we plot \bar{b}_α/\bar{b} and $\delta b_\alpha/\bar{b}$ as a function of $\bar{z}J/U$ along the horizontal dotted line ($\mu/U = 0.8$) in Fig. 3. We note that $\delta b_\alpha/\bar{b}$ is denoted by the length of bars for each \bar{b}_α/\bar{b} . At large $\bar{z}J/U$ far from the phase boundary, \bar{b}_α/\bar{b} is tend to be grouped accompanied by negligibly small $\delta b_\alpha/\bar{b}$. In the limit of $\bar{z}J/U \rightarrow \infty$, \bar{b}_α/\bar{b} is grouped into five classes equivalent to the coordination number, i.e., NoC for $k = 1$. This means that, if correlation effect is small, the coordination number controls physical properties as expected. On the other hand, with approaching $\bar{z}J/U$ to the phase boundary, the mean deviation $\delta b_\alpha/\bar{b}$ becomes large. This means that the number of distinct vertices with different local SF amplitudes increases with approaching the boundary. In other words, long-distant

correlation becomes important to obtain critical behaviors near the phase transition.

To make critical behaviors visible, we introduce a new quantity that can characterize distinct number of vertices more than 27. We use $\langle \hat{b}_i \rangle$ itself for this purpose, and try to find how many distinct values exist with approaching to the phase boundary. For distinguishing different value of local SF amplitude, we (i) make shifting and scaling for $\langle \hat{b}_i \rangle$ to be located within $[0, 1]$. This is done by evaluating $(\langle \hat{b}_i \rangle - \min[\{\langle \hat{b}_i \rangle\}]) / (\max[\{\langle \hat{b}_i \rangle\}] - \min[\{\langle \hat{b}_i \rangle\}])$, where min and max denote minimum and maximum among all values of local SF amplitude, respectively. Then, we (ii) sort the scaled $\langle \hat{b}_i \rangle$ from 0 to 1, (iii) calculate the difference of $\langle \hat{b}_i \rangle$ between i and $i + 1$ from $i = 1$ to $i = N - 1$, and (iv) count the number of the difference (gap) whose magnitude is more than a given small threshold value. We call this number the number of gap (NoG). For example, NoG is zero for the square lattice because $\langle \hat{b}_i \rangle$ is independent of i . In the Penrose lattice, we have NoG = 4 in the large limit of $\bar{z}J/U$ since there are five distinct values of $\langle \hat{b}_i \rangle$. We show log-log plot of NoG in Fig. 4(b) along the horizontal dotted line in Fig. 3, where four different threshold values, 10^{-5} , 5×10^{-6} , 10^{-6} , and 5×10^{-7} are used. With approaching to the phase boundary at $\bar{z}J_c/U \approx 0.0835$, NoG increases, indicating the increase of distinct vertices with different local SF amplitude. Interesting is that, with decreasing the threshold value, NoG rapidly increases near the boundary and shows a diverging behavior with an approximate exponent around -0.9 , i.e., $\text{NoG} \propto (J - J_c)^{-0.9}$. This resembles to a critical behavior toward continuous phase transition as suggested from the vanishing of averaged order parameter \bar{b} [see inset of Fig 4(a)].

To understand this diverging behavior more, we focus on the fact that the increase of NoG corresponds to the increase of distinct vertices with different local SF amplitude. The latter is measured by NoC, whose large region is proportional to $k^{1.84}$ as shown in Fig. 4(c). Therefore, diverging behavior in NoG is directly connected to diverging behavior in NoC at large k . Since k represents the number of links from a given vertex, we may regard k as a measure of correlation length ξ from a given vertex. Based on this reasoning, we have $\text{NoG} \propto \text{NoC} \propto k^{1.84} \propto \xi^{1.84}$. Since $\xi \propto (J - J_c)^{-0.5}$ for the mean-field phase transition, we finally expect that $\text{NoG} \propto (J - J_c)^{-0.92}$, whose exponent is close to the calculated one in NoG, ≈ -0.9 . This indicates that diverging behavior in NoG is a consequence of criticality in the mean-field phase transition. We note that this critical behavior does not appear if $\mu/U = n_0$ and $J/U \rightarrow 0$. We suggest that the assumption of $\xi \propto k$ may change if we alter the class of universality. We leave this to future work.

Usefulness of perpendicular space presentation has already been found in considering magnetism on the Penrose lattice [25,28]. Therefore, we show the perpendicular space representation of $\langle \hat{b}_i \rangle$ in Fig. 5 for two sets of parameters at the end of the red dashed line in Fig. 3. We recognize notable differences in the two cases. For the parameter far from the phase boundary, we find 14 distinct sections in Figs. 5(c) and 5(d). The number corresponds to the number of distinct vertices obtained by setting $k = 1$ as discussed above. On the other hand, for the parameter close to the phase boundary, we can see a fractal structure in Figs. 5(a) and 5(b). For example, we find a various size of star structure inside stars. We can

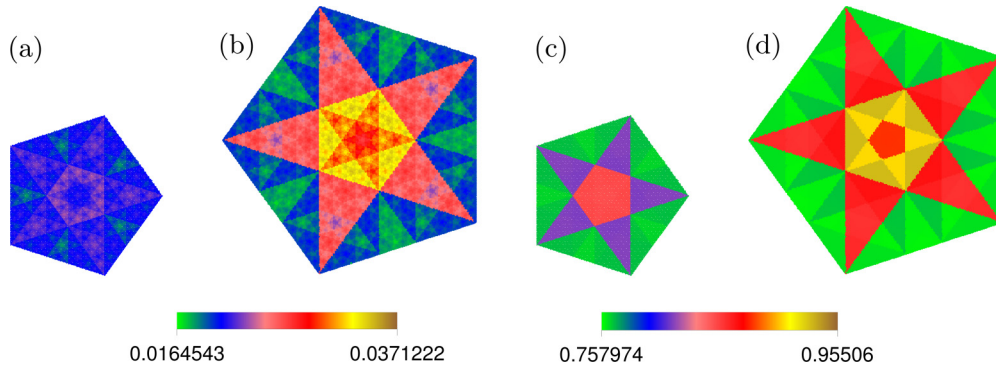


FIG. 5. Representation of vertex local superfluid amplitude in perpendicular space ($\mathcal{Z} = 1, 2$) for (a,b) $(\mu/U, \bar{z}J/U) = (0.8, 0.084)$ and for (c,d) $(\mu/U, \bar{z}J/U) = (0.8, 0.18)$. The numbers in color bars show extremes of local superfluid amplitude for given parameters.

understand the emergence of the fractal structure near the phase transition as follows. Because of diverging behavior in NoG near the MI-SF phase boundary, all distances become relevant. We have found from the previous discussion that tracing far distant links by increasing k enhances NoC dramatically. Therefore, we can expect further distinguishable sections in the perpendicular space, resulting in fractal nature. In other words, a combination of criticality leading to phase transition and aperiodicity is a key for the emergence of fractal structure.

IV. CONCLUSION

We have obtained a mean-field phase diagram in the Penrose-Bose-Hubbard model. We have found that the Penrose lattice does not change the MI-SF boundary drastically in comparison with a square lattice. However, the spatial distribution of a Bose condensate is unequal, and indeed fractal structure appears in the perpendicular representation of local SF amplitude near the MI-SF phase transition. This is a consequence of the cooperative effect of criticality leading to phase transition and quasiperiodicity, which is expected to be a common feature in aperiodic strongly correlated systems.

ACKNOWLEDGMENTS

This work was supported by a Challenging Research Exploratory (Grant No. JP17K18764), Grant-in-Aid for Scientific Research on Innovative Areas (Grant No. JP19H05821).

APPENDIX: PERIODIC BOUNDARY CONDITION AND PERPENDICULAR REPRESENTATION IN PENROSE LATTICE

In this Appendix, we explain how to construct a two-dimensional finite-size Penrose lattice with periodic boundary condition systematically. To make a finite-size Penrose lattice, a cut-and-projection method is well known and established. In this method, we first consider a hypercubic lattice in a five-dimensional space consisting of two-dimensional real space and three-dimensional perpendicular space. Five primitive vectors of the hypercubic lattice are given by

$$\mathbf{e}_i = (\delta_{i,1}, \delta_{i,2}, \delta_{i,3}, \delta_{i,4}, \delta_{i,5}) \quad (i = 1, 2, \dots, 5). \quad (\text{A1})$$

Thus, vertices on the hypercubic lattice are written by $\mathbf{n}_k = \sum_{i=1}^5 n_{k,i} \mathbf{e}_i$, where k is the vertex number and $n_{k,i} \in \mathbb{Z}$. Here, we introduce the real (perpendicular) space as a two-dimensional plane (three-dimensional space) constructed by orthonormal vectors \mathbf{v}_1 and \mathbf{v}_2 ($\mathbf{v}_3, \mathbf{v}_4$ and \mathbf{v}_5) defined by

$$\mathbf{v}_1 = \sqrt{\frac{2}{5}}(1, \cos \phi, \cos 2\phi, \cos 3\phi, \cos 4\phi), \quad (\text{A2})$$

$$\mathbf{v}_2 = \sqrt{\frac{2}{5}}(0, \sin \phi, \sin 2\phi, \sin 3\phi, \sin 4\phi), \quad (\text{A3})$$

$$\mathbf{v}_3 = \sqrt{\frac{2}{5}}(1, \cos 2\phi, \cos 4\phi, \cos \phi, \cos 3\phi), \quad (\text{A4})$$

$$\mathbf{v}_4 = \sqrt{\frac{2}{5}}(0, \sin 2\phi, \sin 4\phi, \sin \phi, \sin 3\phi), \quad (\text{A5})$$

$$\mathbf{v}_5 = \sqrt{\frac{1}{5}}(1, 1, 1, 1, 1), \quad (\text{A6})$$

with $\phi = 2\pi/5$. To project five-dimensional vertices into the real and perpendicular spaces, we use projection matrices,

$$\mathbf{P}_r = \sum_{i=1}^2 \mathbf{e}_i^{(r)} \otimes \mathbf{v}_i, \quad \mathbf{P}_p = \sum_{j=1}^3 \mathbf{e}_j^{(p)} \otimes \mathbf{v}_{j+2}, \quad (\text{A7})$$

where unit vectors in real and perpendicular spaces are given by $\mathbf{e}_i^{(r)} = (\delta_{i,1}, \delta_{i,2})_r$ and $\mathbf{e}_j^{(p)} = (\delta_{j,1}, \delta_{j,2}, \delta_{j,3})_p$ for $i = 1, 2$ and $j = 1, 2, 3$, respectively. By using the projection matrices, the real- and perpendicular-space vertices are obtained by $\mathbf{v}_k^{(r)} = \mathbf{P}_r \mathbf{n}_k = (\mathbf{n}_k \cdot \mathbf{v}_1, \mathbf{n}_k \cdot \mathbf{v}_2)_r$ and $\mathbf{v}_k^{(p)} = \mathbf{P}_p \mathbf{n}_k = (\mathbf{n}_k \cdot \mathbf{v}_3, \mathbf{n}_k \cdot \mathbf{v}_4, \mathbf{n}_k \cdot \mathbf{v}_5)_p$. As confirmed easily, we can find all vertices in a Penrose lattice as the vertices of hypercubic lattice projected into the real space, e.g., five vertices $\mathbf{n}_k = \mathbf{e}_k$ for $k = 1, 2, \dots, 5$ give five apices of pentagon (star) located on the origin.

However, the projected vertices obviously include unwanted vertices for a Penrose lattice. To exclude these unwanted vertices, we use a three-dimensional window in the perpendicular space. The window is a rhombic icosahedron constructed by five vectors $\mathbf{d}_i^{(p)} = \mathbf{P}_p \mathbf{e}_i$; inner space of the window is given by $\mathcal{W} = \{\sum_{i=1}^5 r_i \mathbf{d}_i^{(p)} \mid r_i \in [0, 1)\}$. If a projected vertex into the perpendicular space $\mathbf{P}_p \mathbf{n}_k$ is out of the window, we ignore a projected vertex of \mathbf{n}_k into the real space. Through this procedure, we exclude the unwanted

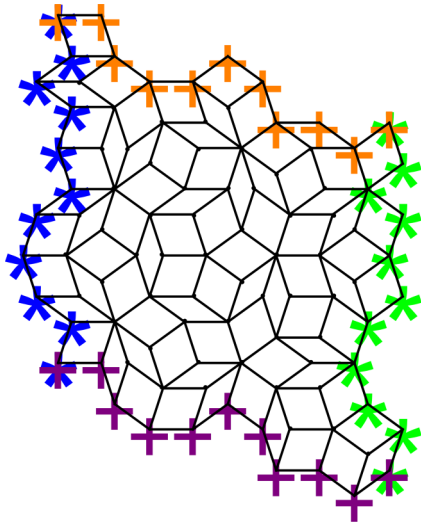


FIG. 6. An approximant of Penrose lattice with an approximated golden ratio $\tau \approx \tau_3 = 3/2$, including $N_v = 76$ vertices in a unit cell. With periodic boundary condition, orange crosses on the upper (green stars on the right) boundaries are identified with purple crosses on the lower (blue stars on the left) boundaries.

vertices for a Penrose lattice [68]. Note that the allowed vertices \mathbf{n}_k are classified into four groups by an integer index $Z = \sqrt{5}\mathbf{n}_k \cdot \mathbf{v}_5 = 1, 2, 3, 4$ corresponding to z component of the perpendicular space, i.e., four planes in the perpendicular space. Therefore, the four planes restricted in the window include all vertices giving a Penrose lattice.

Next, we move to a Penrose lattice with periodic boundary condition, which corresponds to an approximant of a Penrose lattice. To obtain the approximant, we use a multigrid method as follows [64]. In this method, we make a Penrose lattice or its approximant in two steps: (i) find a five-dimensional integer vector $\mathbf{n}(\mathbf{x})$ as a function of two-dimensional real vector \mathbf{x} and (ii) make a vertex of the Penrose lattice or its approximant with $\mathbf{v}^{(r)}(\mathbf{x}) = \mathbf{P}_r \mathbf{n}(\mathbf{x}) = \sum_{i=1}^5 n_i(\mathbf{x}) \mathbf{d}_i^{(r)}$ where $\mathbf{d}_i^{(r)} = \mathbf{P}_r \mathbf{e}_i$. As explained above, if the integer vector $\mathbf{n}(\mathbf{x})$ includes all vectors consisting of arbitrary integers $n_i \in \mathbb{Z}$, unwanted vertices are also included in a Penrose lattice obtained by the step (ii) with $\mathbf{n}(\mathbf{x})$. To exclude unwanted vertices, interestingly, we only

consider the integer vector given by

$$n_i(\mathbf{x}) = \lfloor \mathbf{x} \cdot \mathbf{d}_i^{(r)} - \gamma_i \rfloor, \quad (\text{A8})$$

where the floor function $\lfloor a \rfloor$ denotes the largest integer less than or equal to a , and γ_i is an arbitrary real number satisfying $\sum_{i=1}^5 \gamma_i \in \mathbb{Z}$. In this equation, the floor function gives an integer indexing a neighboring vertex of \mathbf{x} , and γ_i plays the role of window [65]. Therefore, if we search all integer vectors $\mathbf{n}(\mathbf{x})$ in a two-dimensional certain finite space $\mathbf{x} \in \mathcal{S}_r$, we can obtain a finite-size Penrose lattice around the space \mathcal{S}_r . However, this procedure usually requires a careful searching without dropping any vertices. To find the set of integer vectors $\mathbf{n}(\mathbf{x})$ efficiently, we use a recursive algorithm proposed in Ref. [69].

On the other hand, to approximate the Penrose lattice to a periodic lattice, we substitute in Eq. (A8) for the quasiunit vectors $\mathbf{d}_i^{(r)}$ rewritten by

$$\begin{aligned} \mathbf{d}_1^{(r)} &= \sqrt{\frac{2}{5}}(1, 0)_r, \\ \mathbf{d}_2^{(r)} &= \sqrt{\frac{2}{5}}(\cos \phi, \sin \phi)_r, \\ \mathbf{d}_3^{(r)} &= -\mathbf{d}_1^{(r)} + \tau^{-1} \mathbf{d}_2^{(r)}, \\ \mathbf{d}_4^{(r)} &= -\tau^{-1} \{ \mathbf{d}_1^{(r)} + \mathbf{d}_2^{(r)} \}, \\ \mathbf{d}_5^{(r)} &= \tau^{-1} \mathbf{d}_1^{(r)} - \mathbf{d}_2^{(r)}. \end{aligned} \quad (\text{A9})$$

Here, the golden ratio $\tau = (1 + \sqrt{5})/2$ is approximated by a rational number $\tau_n \equiv F_{n+1}/F_n \xrightarrow{n \rightarrow \infty} \tau$, where F_n is the n th Fibonacci number. With the rational number τ_n , the quasiunit vectors give a large unit cell with translational symmetry. Therefore, we obtain an approximant of the Penrose lattice as the unit cell including $N_v = 4F_{2n+1} + 3F_{2n}$ vertices. Figure 6 represents an approximant with $n = 3$, which contains $N_v = 76$ vertices as a unit cell. Note that the upper (right) and lower (left) boundaries of this approximant are connected with periodic boundary condition. In this paper, we consider an approximant of Penrose lattice with $n = 11$, which results in $N_v = 167761$ vertices at most.

-
- [1] D. Shechtman, I. Blech, D. Gratias, and J. W. Cahn, Metallic Phase with Long-Range Orientational Order and no Translational Symmetry, *Phys. Rev. Lett.* **53**, 1951 (1984).
- [2] D. Levine and P. J. Steinhardt, Quasicrystals: A New Class of Ordered Structures, *Phys. Rev. Lett.* **53**, 2477 (1984).
- [3] W. Yao, E. Wang, C. Bao, Y. Zhang, K. Zhang, K. Bao, C. Kai Chan, C. Chen, J. Avila, M. C. Asensio, J. Zhu, and S. Zhou, Quasicrystalline 30° twisted bilayer graphene as an incommensurate superlattice with strong interlayer coupling, *Proc. Natl. Acad. Sci.* **115**, 6928 (2018).
- [4] W. Jin and Y. Gao, Optically induced two-dimensional photonic quasicrystal lattices in iron-doped lithium niobate crystal with an amplitude mask, *Appl. Phys. Lett.* **101**, 141104 (2012).
- [5] W. Steurer, Quasicrystals: What do we know? What do we want to know? What can we know? *Acta Crystallogr. Sect. A* **74**, 1 (2018).
- [6] D. V. Louzguine-Luzgin and A. Inoue, Formation and properties of quasicrystals, *Annu. Rev. Mater. Res.* **38**, 403 (2008).
- [7] K. Kamiya, T. Takeuchi, N. Kabeya, N. Wada, T. Ishimasa, A. Ochiai, K. Deguchi, K. Imura, and N. K. Sato, Discovery of superconductivity in quasicrystal, *Nat. Commun.* **9**, 154 (2018).
- [8] R. N. Araújo and E. C. Andrade, Conventional superconductivity in quasicrystals, *Phys. Rev. B* **100**, 014510 (2019).
- [9] S. Sakai, N. Takemori, A. Koga, and R. Arita, Superconductivity on a quasiperiodic lattice: Extended-to-localized crossover of cooper pairs, *Phys. Rev. B* **95**, 024509 (2017).

- [10] S. Sakai and R. Arita, Exotic pairing state in quasicrystalline superconductors under a magnetic field, *Phys. Rev. Res.* **1**, 022002(R) (2019).
- [11] K. Deguchi, S. Matsukawa, N. K. Sato, T. Hattori, K. Ishida, H. Takakura, and T. Ishimasa, Quantum critical state in a magnetic quasicrystal, *Nat. Mater.* **11**, 1013 (2012).
- [12] J. Otsuki and H. Kusunose, Distributed hybridization model for quantum critical behavior in magnetic quasicrystals, *J. Phys. Soc. Jpn.* **85**, 073712 (2016).
- [13] L.-J. Lang, X. Cai, and S. Chen, Edge States and Topological Phases in One-Dimensional Optical Superlattices, *Phys. Rev. Lett.* **108**, 220401 (2012).
- [14] F. Matsuda, M. Tezuka, and N. Kawakami, Topological properties of ultracold bosons in one-dimensional quasiperiodic optical lattice, *J. Phys. Soc. Jpn.* **83**, 083707 (2014).
- [15] A. Dareau, E. Levy, M. B. Aguilera, R. Bouganne, E. Akkermans, F. Gerbier, and J. Beugnon, Revealing the Topology of Quasicrystals with a Diffraction Experiment, *Phys. Rev. Lett.* **119**, 215304 (2017).
- [16] S. Spurrier and N. R. Cooper, Theory of quantum oscillations in quasicrystals: Quantizing spiral Fermi surfaces, *Phys. Rev. B* **100**, 081405(R) (2019).
- [17] H. Huang and F. Liu, Quantum Spin Hall Effect and Spin Bott Index in a Quasicrystal Lattice, *Phys. Rev. Lett.* **121**, 126401 (2018).
- [18] R. Ghadimi, T. Sugimoto, and T. Tohyama, Majorana zero-energy mode and fractal structure in Fibonacci-Kitaev chain, *J. Phys. Soc. Jpn.* **86**, 114707 (2017).
- [19] M. A. Bandres, M. C. Rechtsman, and M. Segev, Topological Photonic Quasicrystals: Fractal Topological Spectrum and Protected Transport, *Phys. Rev. X* **6**, 011016 (2016).
- [20] P. Ma and Y. Liu, Inflation rules, band structure, and localization of electronic states in a two-dimensional Penrose lattice, *Phys. Rev. B* **39**, 9904 (1989).
- [21] N. G. de Bruijn, Algebraic theory of penrose's non-periodic tilings of the plane. I, *Indagationes Mathematicae (Proceedings)* **84**, 39 (1981).
- [22] N. G. de Bruijn, Algebraic theory of Penrose's non-periodic tilings of the plane. II, *Indagationes Mathematicae (Proceedings)* **84**, 53 (1981).
- [23] J. Oitmaa, M. Aydin, and M. J. Johnson, Antiferromagnetic Ising model on the Penrose lattice, *J. Phys. A: Math. Gen.* **23**, 4537 (1990).
- [24] Y. Liu and P. Ma, Electronic properties of two-dimensional quasicrystals with near-neighbor interactions, *Phys. Rev. B* **43**, 1378 (1991).
- [25] A. Szallas and A. Jagannathan, Spin waves and local magnetizations on the Penrose tiling, *Phys. Rev. B* **77**, 104427 (2008).
- [26] P. Vignolo, M. Bellec, J. Böhm, A. Camara, J.-M. Gambaudo, U. Kuhl, and F. Mortessagne, Energy landscape in a Penrose tiling, *Phys. Rev. B* **93**, 075141 (2016).
- [27] N. Takemori and A. Koga, DMFT study of the local correlation effects in quasi-periodic system, *J. Phys.: Conf. Ser.* **592**, 012038 (2015).
- [28] A. Koga and H. Tsunetsugu, Antiferromagnetic order in the Hubbard model on the Penrose lattice, *Phys. Rev. B* **96**, 214402 (2017).
- [29] N. Takemori, A. Koga, and H. Hafermann, Intersite electron correlations on inhomogeneous lattices: a real-space dual fermion approach, [arXiv:1801.02441](https://arxiv.org/abs/1801.02441).
- [30] A. Jagannathan, Quasiperiodic Heisenberg antiferromagnets in two dimensions, *Eur. Phys. J. B* **85**, 68 (2012).
- [31] A. Szallas, A. Jagannathan, and S. Wessel, Phason-disordered two-dimensional quantum antiferromagnets, *Phys. Rev. B* **79**, 172406 (2009).
- [32] Y. Murakami, D. Golež, T. Kaneko, A. Koga, A. J. Millis, and P. Werner, Collective modes in excitonic insulators: Effects of electron-phonon coupling and signatures in the optical response, *Phys. Rev. B* **101**, 195118 (2020).
- [33] M. Arai, T. Tokihiro, T. Fujiwara, and M. Kohmoto, Strictly localized states on a two-dimensional Penrose lattice, *Phys. Rev. B* **38**, 1621 (1988).
- [34] T. Fujiwara, M. Arai, T. Tokihiro, and M. Kohmoto, Localized states and self-similar states of electrons on a two-dimensional Penrose lattice, *Phys. Rev. B* **37**, 2797 (1988).
- [35] I. Bloch, Ultracold quantum gases in optical lattices, *Nat. Phys.* **1**, 23 (2005).
- [36] K. Singh, K. Saha, S. A. Parameswaran, and D. M. Weld, Fibonacci optical lattices for tunable quantum quasicrystals, *Phys. Rev. A* **92**, 063426 (2015).
- [37] L. Guidoni, C. Triché, P. Verkerk, and G. Grynberg, Quasiperiodic Optical Lattices, *Phys. Rev. Lett.* **79**, 3363 (1997).
- [38] L. Sanchez-Palencia and L. Santos, Bose-Einstein condensates in optical quasicrystal lattices, *Phys. Rev. A* **72**, 053607 (2005).
- [39] T. A. Corcovilos and J. Mittal, Two-dimensional optical quasicrystal potentials for ultracold atom experiments, *Appl. Opt.* **58**, 2256 (2019).
- [40] J. Hou, H. Hu, K. Sun, and C. Zhang, Superfluid-Quasicrystal in a Bose-Einstein Condensate, *Phys. Rev. Lett.* **120**, 060407 (2018).
- [41] S. Gopalakrishnan, I. Martin, and E. A. Demler, Quantum Quasicrystals of Spin-Orbit-Coupled Dipolar Bosons, *Phys. Rev. Lett.* **111**, 185304 (2013).
- [42] M. P. A. Fisher, P. B. Weichman, G. Grinstein, and D. S. Fisher, Boson localization and the superfluid-insulator transition, *Phys. Rev. B* **40**, 546 (1989).
- [43] O. Dutta, M. Gajda, P. Hauke, M. Lewenstein, D.-S. Lühmann, B. A. Malomed, T. Sowiński, and J. Zakrzewski, Non-standard Hubbard models in optical lattices: A review, *Rep. Prog. Phys.* **78**, 066001 (2015).
- [44] D. Jaksch, C. Bruder, J. I. Cirac, C. W. Gardiner, and P. Zoller, Cold Bosonic Atoms in Optical Lattices, *Phys. Rev. Lett.* **81**, 3108 (1998).
- [45] M. Greiner, O. Mandel, T. Esslinger, T. W. Hänsch, and I. Bloch, Quantum phase transition from a superfluid to a Mott insulator in a gas of ultracold atoms, *Nature* **415**, 39 (2002).
- [46] T. Giamarchi, C. Rüegg, and O. Tchernyshyov, Bose-Einstein condensation in magnetic insulators, *Nat. Phys.* **4**, 198 (2008).
- [47] T. Nikuni, M. Oshikawa, A. Oosawa, and H. Tanaka, Bose-Einstein Condensation of Dilute Magnons in TiCuCl_3 , *Phys. Rev. Lett.* **84**, 5868 (2000).
- [48] C. Bruder, R. Fazio, and G. Schön, Superconductor-Mott-insulator transition in Bose systems with finite-range interactions, *Phys. Rev. B* **47**, 342 (1993).
- [49] K. Viebahn, M. Sbroscia, E. Carter, J.-C. Yu, and U. Schneider, Matter-Wave Diffraction from a Quasicrystalline Optical Lattice, *Phys. Rev. Lett.* **122**, 110404 (2019).
- [50] D. Johnstone, P. Öhberg, and C. W. Duncan, Mean-field phases of an ultracold gas in a quasicrystalline potential, *Phys. Rev. A* **100**, 053609 (2019).

- [51] R. V. Pai, J. M. Kurdestany, K. Sheshadri, and R. Pandit, Bose-Hubbard models in confining potentials: Inhomogeneous mean-field theory, *Phys. Rev. B* **85**, 214524 (2012).
- [52] J. M. Kurdestany, R. V. Pai, and R. Pandit, The inhomogeneous extended Bose-Hubbard model: A mean-field theory, *Ann. Phys.* **524**, 234 (2012).
- [53] P. Pisarski, R. M. Jones, and R. J. Gooding, Application of a multisite mean-field theory to the disordered Bose-Hubbard model, *Phys. Rev. A* **83**, 053608 (2011).
- [54] T. McIntosh, P. Pisarski, R. J. Gooding, and E. Zaremba, Multi-site mean-field theory for cold bosonic atoms in optical lattices, *Phys. Rev. A* **86**, 013623 (2012).
- [55] A. Barman and S. Basu, Phase diagram of trapped bosons in a kagome lattice—application of inhomogeneous mean field theory, *J. Phys. B: At., Mol. Opt. Phys.* **47**, 025302 (2014).
- [56] S. Yi, T. Li, and C. P. Sun, Novel Quantum Phases of Dipolar Bose Gases in Optical Lattices, *Phys. Rev. Lett.* **98**, 260405 (2007).
- [57] K. Sheshadri, H. R. Krishnamurthy, R. Pandit, and T. V. Ramakrishnan, Percolation-Enhanced Localization in the Disordered Bosonic Hubbard Model, *Phys. Rev. Lett.* **75**, 4075 (1995).
- [58] A. E. Niederle and H. Rieger, Bosons in a two-dimensional bichromatic quasiperiodic potential: Analysis of the disorder in the Bose-Hubbard parameters and phase diagrams, *Phys. Rev. A* **91**, 043632 (2015).
- [59] D. S. Rokhsar and B. G. Kotliar, Gutzwiller projection for bosons, *Phys. Rev. B* **44**, 10328 (1991).
- [60] W. Krauth, M. Caffarel, and J.-P. Bouchaud, Gutzwiller wave function for a model of strongly interacting bosons, *Phys. Rev. B* **45**, 3137 (1992).
- [61] T. Ohgoe, T. Suzuki, and N. Kawashima, Ground-state phase diagram of the two-dimensional extended Bose-Hubbard model, *Phys. Rev. B* **86**, 054520 (2012).
- [62] M. Iskin, Route to supersolidity for the extended Bose-Hubbard model, *Phys. Rev. A* **83**, 051606(R) (2011).
- [63] O. Entin-Wohlman, M. Kléman, and A. Pavlovitch, Penrose tiling approximants, *J. Phys.* **49**, 587 (1988).
- [64] F. Babalievski and O. Peshev, An algorithm to construct quasilattices and study percolation on them, *Comput. Phys. Commun.* **60**, 27 (1990).
- [65] H. Tsunetsugu, T. Fujiwara, K. Ueda, and T. Tokihiro, Electronic properties of the penrose lattice. i. energy spectrum and wave functions, *Phys. Rev. B* **43**, 8879 (1991).
- [66] D. van Oosten, P. van der Straten, and H. T. C. Stoof, Quantum phases in an optical lattice, *Phys. Rev. A* **63**, 053601 (2001).
- [67] J. K. Freericks and H. Monien, Phase diagram of the Bose-Hubbard model, *Europhys. Lett.* **26**, 545 (1994).
- [68] M. Senechal, *Quasicrystals and Geometry* (Cambridge University Press, New York, 1996).
- [69] F. V. Babalievski, Percolation conductivity of penrose lattices by the transfer-matrix monte carlo method, *J. Non-Cryst. Solids* **153-154**, 370 (1993).